Synergized selenium-vacancy heterogeneous interface and carbon nanotubes for insight into efficient oxidation of pollutants via photocatalytic peroxymonosulfate activation

Yuxuan He [a,b], Jin Qian [a,b,*], Peifang Wang [a,b], Taiping Xie [c], Dionysios D. Dionysiou [d], Bianhe Lu [a,b], Sijing Tang [a,b]

[a] *Key Laboratory of Integrated Regulation and Resource Development on Shallow Lakes, Ministry of Education, Hohai University, Nanjing 210098, People's Republic of China*
[b] *College of Environment, Hohai University, Nanjing 210098, People's Republic of China*
[c] *School of Materials Science and Engineering, Yangtze Normal University, Chongqing 408100, People's Republic of China*
[d] *Environmental Engineering and Science Program, Department of Chemical and Environmental Engineering (DCEE), 705 Engineering Research Center, University of Cincinnati, Cincinnati, OH 45221-0012, United States*

ARTICLE INFO

ABSTRACT

Advanced strategies for enhancing catalytic performance of catalysts include multi-metal active site exposure, vacancy growth and electronic structure optimization. Here, carbon nanotube-loaded $CoSe_2/FeSe_2$ catalysts (Co/Fe-CNT) with multiphase boundaries and embedded selenium vacancies (V_{Se}) were prepared using a one-step hydrothermal method. The catalysts feature unique electronic structures and abundant active sites, and were found to exhibit unexpectedly high activity and stability in photocatalytic mediated sulphate radical (SR-photo) system, with impressive oxidation capacity for complex matrix polluted water. The spontaneously formed internal electric field strongly promoted charge transport and significantly enhanced the photocatalytic property. The V_{Se} formed at the heterogeneous interface could modulate the surface electronic structure and accelerate the redox cycling of transition metals, thereby accelerating the production of reactive oxygen species and boosting the efficiency of contaminant degradation. This work provides guidance for the design of high-performance catalysts for V_{Se} engineering and expands their potential for application in wastewater purification.

1. Introduction

Due to the misuse of antibiotics, water pollution has emerged as a critical environmental issue that seriously endangers human health and social progress. As a result, there has been a significant surge in the need for better water quality [1,2]. Sulphate radical-advanced oxidation processes (SR-AOP) have been widely studied for environmental remediation applications because of their efficiency and wide applicability [3,4]. Compared to the $^{\bullet}OH$-based Fenton process, the SR-AOP offers a wider pH range (pH = 2.0–9.0), enabling the swift elimination of refractory pollutants. And the half-life of $SO_4^{\bullet-}$ (30–40 μs) is longer than that of $^{\bullet}OH$ radical, with a similar standard oxidation potential (E^0 = 2.5–3.1 eV) to $^{\bullet}OH$ radical (half-life = 20 ns; E^0 = 1.8–2.7 eV) [5]. In particular, peroxymonosulfate (PMS) (HSO_5^-) has an asymmetrical

molecular structure and the O-O bond in HSO_5^- is more easily broken to produce reactive oxide species (ROS) than that in peroxydisulfate (PDS) ($S_2O_8^{2-}$). Lately, there has been a quick adoption of the photocatalytic mediated sulphate radical (SR-photo) process as an effective and swift approach for environmental remediation. [6,7]. In the SR-photo system, the generation of sulphate radical ($SO_4^{\bullet-}$) and hydroxyl radicals ($^{\bullet}OH$) by PMS can be activated by photogenerated electrons, which consumption further facilitates photogenerated hole electron pair separation [8]. Meanwhile, the presence of $O_2^{\bullet-}$ in the reaction system can also boost the degradation of pollutants [9]. There is no doubt that catalysts with high electron transfer capacity and certain photocatalytic effects are of enormous use. Therefore, the construction of SR-photo systems is an effective way to enhance the performance of pollutant removal.

The flourishing development of nanotechnology and nanomaterials

---

provides access to the field of photocatalysis for PMS activation at nanoscale heterogeneous interfaces, providing underlying insights and utility tools for ROS in a variety of applications [10,11]. Metal-based nanoparticles containing Fe, Mn, Co, or Cu have demonstrated remarkable proficiency in activating PMS and have been extensively studied [12–14]. Although these nanoparticles are highly efficient for the activation of PMS, the leaching of poisonous metal ions remains an issue of concern [15]. Metal-free catalysts mainly rely on non-radical pathways as the mainstream for pollutant degradation. However, these pathways generate ROS with low oxidation potentials, which leads to less efficient mineralization of pollutants and limited applications [16]. Therefore, advanced catalysts/activators that combine high efficiency, economy and sustainability need to be further explored.

A versatile class of nanomaterials, transition metal selenides (TMS) have been broadly investigated in oxygen evolution reaction, hydrogen production, energy conversion and storage [17,18]. Especially $FeSe_2$, a major member of selenides, is extensively used in energy generation due to its superior reactivity and durability [19]. Hence, it is a suitable choice for application of $FeSe_2$ in the field of environmental catalysis. However, the slow reaction rate of $FeSe_2$ significantly constrains its practical applicability for PMS activation. Additionally, due to the long reaction time, the leaching of metal ions becomes a key environmental concern for $FeSe_2$ application, which in turn affects the lifetime of $FeSe_2$ [20]. Therefore, it is essential to reasonably design and synthesize $FeSe_2$-based composites with excellent electron transport kinetics, endurance, and satisfactory catalytic stability.

The construction of heterojunctions is considered to be one of the most powerful strategies for facilitating internal charge migration and transfer [21]. A locally built-in electric field can be generated spontaneously at the interface via the heterogeneous boundary, thereby facilitating charge migration and conduction [22]. Moreover, the phase interface in a heterojunction tends to induce lattice mismatch and distortion, resulting in the creation of vacancies in the catalyst [23]. $CoSe_2$, which has the best $t_{2g}^6 e_g^1$ electronic configuration, is certainly a strong choice for improving the internal electric field and reaction kinetics [24]. Similarly, $CoSe_2$ has excellent catalytic activity as another TMS [25]. Moreover, the combination of metals with different electronegativities can cause the formation of vacancies more easily [26]. The introduction of vacancies results in the rearrangement of excess electrons around specific metal atoms, and accelerate the redox cycle between active metals [27,28]. Furthermore, structures with vacancies can subtly modulate the local coordination environment to enhance the adsorption energy of the oxidant on the catalyst surface. Therefore, the cobalt-iron-selenide composites will be a vacancy-rich and satisfactory catalyst. On the other hand, carbon nanomaterials are often introduced to enhance catalyst stability and tune electron transfer [29,30]. Carbon nanotubes (CNTs), with unique nanoparticle growth along tubular networks, not only improve the mechanical stability of the composite, but also promote charge transfer efficiency when working in harsh media for long periods [31]. In composite structures, the surface metals are susceptible to damage by forming ionic states during redox cycling. The CNTs can act to accelerate charge transfer and protect the metals from loss as far as possible. Further, the carbonaceous material can effectively mitigate volume fluctuations and prevent agglomeration of the catalyst during the reaction [32].

Herein, the CNTs-loaded $CoSe_2/FeSe_2$ catalysts (labelled Co/Fe-CNT) with the heterogeneous interface and embedded selenium vacancies were prepared by selenization and hydrothermal methods, and further for SR-photo system. The target contaminant for this work was levofloxacin (LVF), a fluoroquinolone antibiotic that is commonly used to treat severe bacterial infections and is frequently detected in surface and groundwater. Surface chemical state and structural analysis revealed that the obtained Co/Fe-CNT was composed of nanorods embedded with crystal-like structures ($CoSe_2/FeSe_2$) and nanotubes, with CNTs scattered interspersed on each crystal cluster. The catalytic performance of Co/Fe-CNT for the SR-photo system was investigated under solar simulator. By batch experiments, 1Co/1Fe-CNT showed excellent activity, and the reaction rate constant for the light/PMS-activated degradation of LVF was twice as for under the PMS-activated system. The catalyst was stable, and the metal leaching rate was much lower than that of the unloaded CNTs composite (only about 1/5 of 1Co/1Fe). Further investigations including UV-Visible scattering reflectance spectroscopy, electrochemical tests, electron paramagnetic resonance (EPR), radical quenching and theoretical calculations were carried out to explore the electron transfer process inside the heterojunction. In addition, the activation mechanism of Co/Fe-CNT on PMS was uncovered. The optimization of Co/Fe-CNT enhanced the adsorption of PMS on its surface and promoted the transfer of charge from the active sites to the PMS, thereby obtaining higher catalytic activity.

2. Experimental

2.1. Materials

Unless otherwise mentioned, all reagents used in this study were of analytical reagent grade and were used without additional purification. Cobalt nitrate hexahydrate ($Co(NO_3)_2 \cdot 6\ H_2O$), ferric nitrate nonahydrate ($Fe(NO_3)_3 \cdot 9\ H_2O$), Se powder, hydrazine hydrate (N_2H_6O), carbon nanotubes (CNTs), potassium peroxymonosulfate (PMS, $2KHSO_5 \cdot KHSO_4 \cdot K_2SO_4$), levofloxacin (LVF), trimethoprim (TTP), ciprofloxacin (CFX), sulfamethoxazole (SMX), humic acid (HA), methyl alcohol (Meth, CH_4O), tert-butyl alcohol (TBA, $C_4H_{10}O$), L-histidine, furfuryl alcohol (FFA), p-benzoquinone (p-BQ), sodium oxalate ($Na_2C_2O_4$), 5,5-dimethyl-1-pyrroline-N-oxide (DMPO) and 2,2,6,6-tetramethyl-4-piperidine (TEMP) were purchased from Aladdin Chemical Reagent Co. Ltd. H_2SO_4, NaOH, NaCl, $NaNO_3$ and $NaHCO_3$ were purchased from Sinopharm Chemical Reagent Co. Ltd (Shanghai, China). All the aqueous solutions were prepared by using Milli-Q water.

2.2. Catalysts preparation

To prepare a typical catalyst (Fig. 1), a 1:1 molar ratio of $Co(NO_3)_2 \cdot 6\ H_2O$ and $Fe(NO_3)_3 \cdot 9\ H_2O$ were simultaneously dissolved in pure water and mixed thoroughly. Afterward, Se powder with twice the mass of the metal source was added into a certain amount of hydrazine hydrate, and mixed until the Se dissolved completely. Subsequently, the two above solutions were thoroughly stirred and mixed, and the CNTs with a theoretical selenide mass ratio of 0.1 to selenide was added and ultrasonically dispersed for 20 min. The final mixture was transferred to an autoclave and prepared hydrothermally at 180 °C for 24 h. After thorough washing with water and ethanol, and vacuum drying, the catalyst $CoSe_2/FeSe_2$-CNT (Co/Fe-CNT) was obtained. On account of different molar ratios of $Co(NO_3)_2 \cdot 6\ H_2O$ and $Fe(NO_3)_3 \cdot 9\ H_2O$, the corresponding products were denoted as nCo/mFe-CNT (n, m = 1 or 2), accordingly. To allow for comparison, the single phase of pure $CoSe_2$ and $FeSe_2$ were obtained under similar conditions, using onefold $Co(NO_3)_2 \cdot 6\ H_2O$ or $Fe(NO_3)_3 \cdot 9\ H_2O$ as the source.

2.3. Characterization

Powder X-ray diffraction patterns were collected on SmartLab (XRD, Rigaku) equipped with Cu-Kα ($\lambda = 1.54$ Å) radiation at a scanning rate of 3°/min over the range of 2°– 80° (2θ). The morphology was characterized by a field-emission scanning electron microscope (SEM, Zeiss Sigma 300) and high-resolution transmission electron microscope (TEM, JEOL, JEM-2100 F) with an acceleration voltage of 100 kV. The specific surface area was analyzed by N_2 adsorption-desorption isotherms (ASAP 2460, Micromeritics). X-ray photoelectron spectroscopy measurements were taken in 250 xi (XPS, Thermo ESCALAB) using a monochromatic Al Kα X-ray source. UV-Vis diffuse reflectance spectroscopy (DRS) spectra were acquired through PE Lambda 950 spectrophotometer with reference of $BaSO_4$. Solid state electron paramagnetic resonance (EPR)
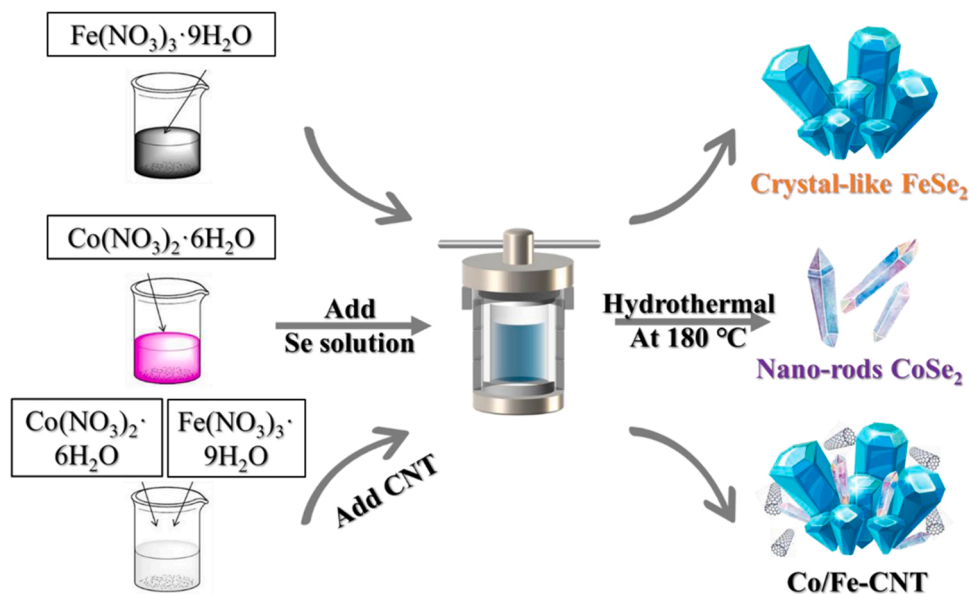
Fig. 1. Schematic illustration for the fabrication process of Co/Fe-CNT.

spectra were obtained on EMXplus-6/1, Bruker, in the X-band (9.85 GHz) with 4.00 G modulation amplitude and a magnetic field modulation of 100 kHz. The concentrations of cobalt and iron ions in reaction solution were quantified by inductively coupled plasma optical emission spectrometry (ICP-OES, PerkinElmer 8300). The total organic carbon (TOC) was measured on Vario TOC. The free radicals ($SO_4^{\bullet-}$, $^{\bullet}OH$ and $O_2^{\bullet-}$) and singlet oxygen ($^1O_2$) were detected on an electron paramagnetic resonance (EPR) spectrometer (Bruker A300, Germany).

2.4. Photoelectrochemical measurements

The electrochemical workstation (CIMPS, Zahner, Germany) was employed for electrochemical analysis. All the experiments were conducted with three-electrode-cell configuration including a working electrode, a platinum electrode as counter electrode, and an Ag/AgCl electrode as the reference electrode. A 300 W xenon lamp was used as light source. Electrochemical impedance spectroscopy (EIS) of Nyquist plots using catalyst-coated ITO conductive glass electrode as working electrode, which were measured in aqueous Na_2SO_4 solution (0.5 M). Mott-Schottky (M-S) measurement was performed to investigate the energy band position of the catalysts, and all M-S plots were carried out at 10 KHz frequency in the dark.

2.5. Experimental procedure and analytical methods

The catalytic performance was assessed at 25 °C using a water bath. Since the degradation efficiency of LVF at 1000 ug/L was particularly rapid that the degradation process could not be observed in the SR-photo system by the catalyst of this work (Fig. S1), the design of the further experiments increased the concentration of LVF. Typically, 20 mg catalyst was added into 100 mL reaction solution ([LVF] = 10 mg/L, pH = 6.89) and stirred for 15 min to establish the adsorption-desorption equilibrium under dark. Afterwards, the reaction sample was exposed to radiation from the solar simulator (Xenon lamp (300 W m^{-2})) accompanying the addition of a certain amount of PMS. At predetermined time intervals, 1.5 mL reaction solution was filtered through a polyether sulfone membrane (pore size 0.22 μm), and quenched with excessive Meth for subsequent analysis. After the LVF degradation by Co/Fe-CNT/PMS/light system, the catalyst was collected and washed with ethanol and pure water three times for the reuse tests. Measurement of LVF concentrations was carried out with a visible-ultraviolet

spectrophotometer (Nanjing Philo Instruments Co. Ltd. model) scanning at 289 nm. Ultraperformance liquid chromatography-quadrupole time of flight premier mass spectrometer (UPLC-QTOF-MS/MS, Agilent 6500, USA) was employed to detect the degradation intermediates.

The multi-pollutant degradation experiment was similar to the above operation, except that the pollutant concentration was different ([LVF] = [TPP] = [CFX] = [SMX] = 5 mg/L).

For the analysis of the contribution of radicals ($SO_4^{\bullet-}$, $^{\bullet}OH$ and $O_2^{\bullet-}$), non-radical ($^1O_2$) and h$^+$ under the degradation reaction, Meth, TBA, p-BQ, L-histidine, FFA and $Na_2C_2O_4$ were selected as chemical quenchers, respectively.

2.6. Toxicity analysis

Ecological Structure Activity Relationships (ECOSAR) procedure was used to analyze the acute and chronic toxicities of LVF and its degradation intermediates. The other analysis methods were provided in Supporting Information.

3. Results and discussion

3.1. Characterization analysis

Fig. 2(a-c) showed SEM images of FeSe$_2$, CoSe$_2$ and 1Co/1Fe-CNT, where the composites retained the crystal-like bulk structure, accompanied by rods of nano-flowers and slender CNTs. The TEM image reflected the interwoven state of the composite 1Co/1Fe-CNT. Additionally, high resolution transmission electron microscopy (HRTEM) image (Fig. 2f) showed that CNTs with a thickness of 6–7 nm was attached between the crystalline nanocrystals [[33], which proved that the CNTs was successfully dispersed in the composite structure. The unique CNTs layer enables accelerated electron transport kinetics. HRTEM image also showed two lattice fringes for FeSe$_2$ with the (211) plane (0.19 nm) and CoSe$_2$ with the (120) plane (0.25 nm). As seen through the Fig. 2e, the composite represented by above two lattice fringes extended into the superimposed portion and were tightly bound, suggesting the generation of the heterojunction between FeSe$_2$ and CoSe$_2$. Further confirmation of the well-grown composite with the formation of a crystal/nanorod interlayer structure was demonstrated by the corresponding energy-dispersive X-ray spectroscopy (EDS) mapping of Co, Fe and Se (Fig. 2g).
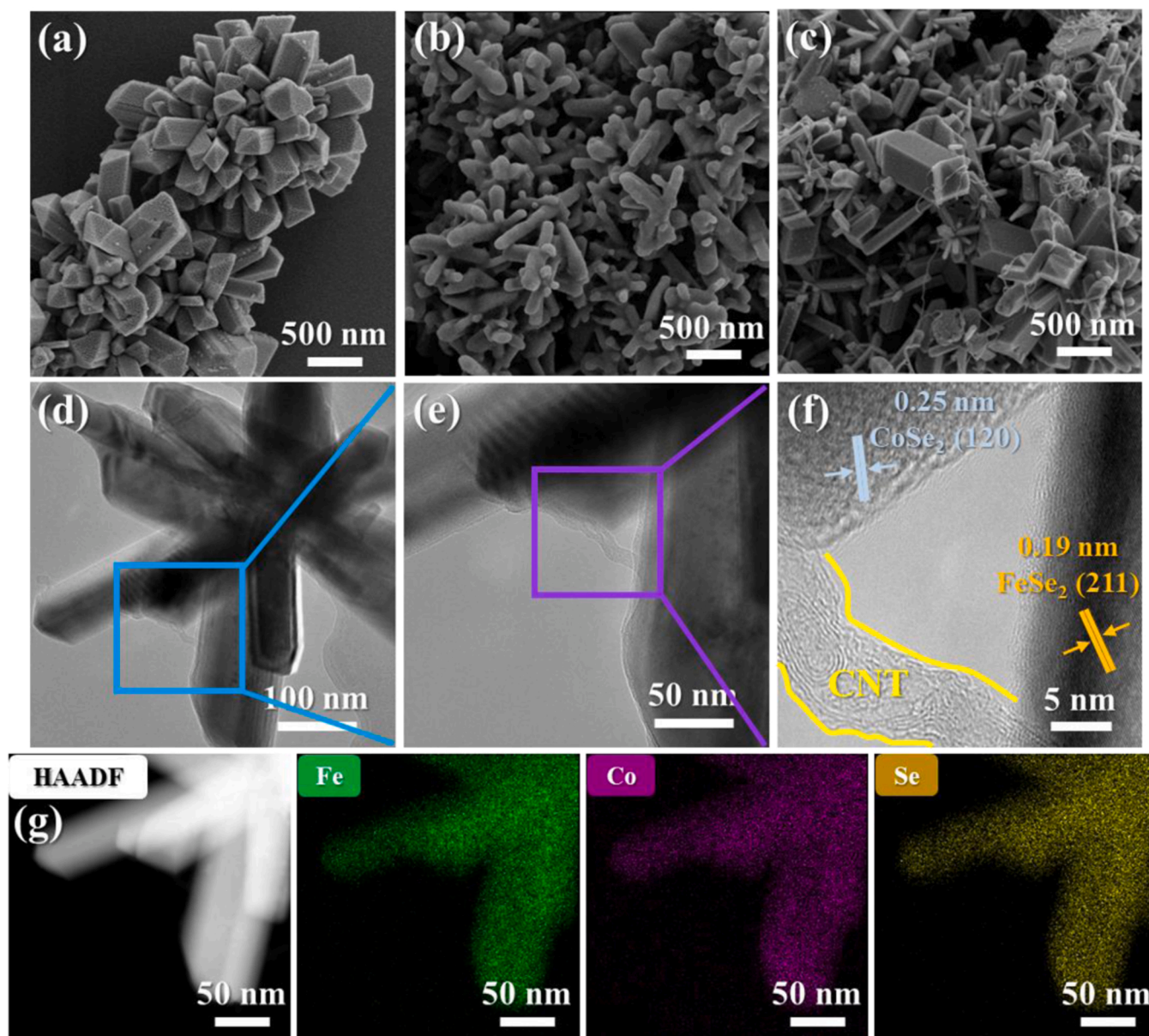
Fig. 2. SEM image of (a) pure CoSe$_2$, (b) pure FeSe$_2$ and (c) 1Co/1Fe-CNT. (d-e) TEM image and (f) HRTEM image of 1Co/1Fe-CNT. (g) Elemental mappings of 1Co/1Fe-CNT including Fe, Co and Se.

The crystal structure of the composites was analyzed by X-ray diffraction (XRD) analysis. In Fig. 3a, the characteristic peaks appearing in CoSe$_2$ and FeSe$_2$ were in excellent match with the standard patterns of JCPDF No. 53-0449 and JCPDF No. 65-1455, indicating that no impurities were presented in the synthesis of the catalysts. Interestingly, the two main diffraction peaks of CoSe$_2$ and FeSe$_2$ at 32°–38° (plot on the Fig. 3a right) were observed, which showed that different ratios of Fe/Co sources resulted in different crystalline phases. In catalyst with more Fe sources (1Co/2Fe-CNT), the crystalline phase was more dominant at 2θ degrees of 34.83° and 36.22°, whereas the intensity of the characteristic peaks at 34.52° and 35.96° was stronger in the catalyst with mainly Co sources (2Co/1Fe-CNT). Composites with the same molar ratio of Fe/Co sources (1Co/1Fe and 1Co/1Fe-CNT) exhibited equal intensity of the characteristic peaks within 32°–38°. Besides, the characteristic peak of pure CNTs was at 25.89°, but it was not observed in the XRD pattern of composites, which proved that the loading of CNTs was quite low on the metal selenides. The pore structures and specific surface area of the pure CoSe$_2$, FeSe$_2$ and the composites were obtained by N$_2$ adsorption-desorption analysis. From the Fig. 3b, the prepared composites displayed type IV isotherm, indicating the existence of mesoporous structures [34]. Based on Brunauer-Emmett-Teller calculations, the surface area of FeSe$_2$ and CoSe$_2$ were only 11.4 and 12.1 m^2/g and that of 1Co/1Fe was only 22.1 m^2/g. By loading with CNTs, the surface area of 1Co/1Fe-CNT increased to 78.7 m^2/g. This result indicated that the increase in the specific surface area of the 1Co/1Fe-CNT catalyst was mainly due to CNTs, which supported the rapid adsorption-activation of PMS.

The binding energy shifts of the Fe and Co species in samples were analyzed by using X-ray photoelectron spectroscopy (XPS). The full-range scan of catalysts was displayed in Fig. S2. The XPS plots for Co 2p and Fe 2p were shown in Fig. 3c, d. The characteristic peaks of the Co species at 778.9 and 793.8 eV were attributed to Co 2p$_{3/2}$ and Co 2p$_{1/2}$, respectively [35,36]. The accompanying convoluted peaks were attributed to Co^{2+} and Co^{3+}, as well as two satellite peaks at 783.8 and 801.9 eV. The contribution of the Co ion in Co/Fe-CNT resulted in partial oxidation compared to pure CoSe$_2$. Driven by the internal electric
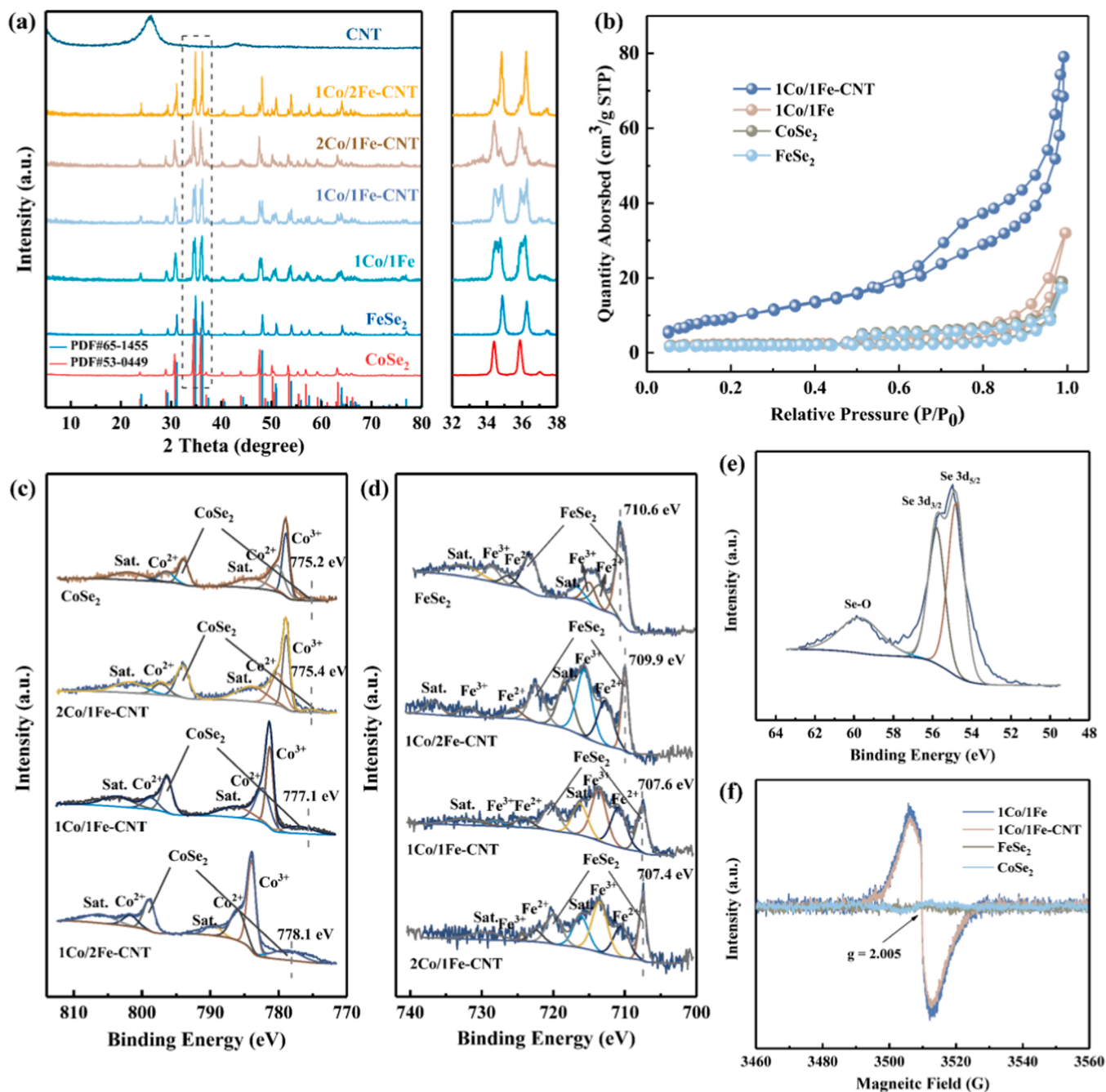
Fig. 3. (a) XRD patterns and (b) N$_2$ adsorption-desorption isotherms of the as-prepared catalysts. (c) Co 2p and (d) Fe 2p XPS spectra of the as-prepared catalysts. (e) Se 3d XPS spectra of 1Co/1Fe-CNT. (f) EPR spectra of as-prepared catalysts.

field generated by the heterojunction, the main peak of Co 2p$_{3/2}$ shifted significantly towards higher binding energies, confirming the existence of strong electronic interactions between the CoSe$_2$ and FeSe$_2$. It was obvious that the more the Fe source was incorporated, the more strongly the Co was oxidized. Besides, a similar phenomenon occurred for Fe 2p [37]. The binding energy of Fe 2p$_{3/2}$ for Co/Fe-CNT was lower than that of pure FeSe$_2$, which indicated the presence of some electron-deficient Se atoms in Co/Fe-CNT. In the Se 3d spectrum (Fig. 3e), peaks at 54.3 and 55.7 eV could be assigned to the energy levels of Se 3d$_{5/2}$ and Se 3d$_{3/2}$, respectively [38]. The binding energy at 59.6 eV represented the Se-O bond, which was attributed to a chemical reaction between oxygen and a small part of residual metalloid Se [39]. The C 1 s spectrum of 1Co/1Fe-CNT (Fig. S3) at 284.3 eV, 284.8 eV and 285.8 eV were classified as C-C, C=C and C-O bonds, respectively, which were typical

structures of CNTs [40].

The solid-state electron paramagnetic resonance measurements were employed to validate the Se vacancies presence in the prepared composites (Fig. 3f). 1Co/1Fe showed a significant EPR signal at g = 2.005, suggesting that electrons were captured from Se vacancies [41]. The result demonstrated that lattice mismatch and lattice distortion were the main causes of Se vacancies when two cations were simultaneously present within crystal structure. In addition, the electronegativity of metallic iron (1.83) was less than that of metallic cobalt (1.88), meaning that selenium was more readily bound to cobalt, and thus led to the construction of heterogeneous structures and the formation of selenium vacancies in FeSe$_2$ [42]. Notably, the EPR signal peak did not change after the introduction of CNTs into the composite, which proved that CNTs had no impacts on the generation of Se vacancies, as well as

indicated that the promising method for generating Se vacancies was the construction of heterogeneous phases in transition metal selenides.

3.2. Photocatalytic activity of catalysts

The optical absorption spectra of the prepared pure monomers and composites were explored by UV-Visible scattering reflectance spectroscopy (UV-Vis DRS) (Fig. 4a). Due to the narrow band gap, $CoSe_2$ and $FeSe_2$ showed strong and stable light absorption in almost all UV–visible range, confirming their excellent absorption and utilization of full spectrum. The composites displayed the absorption curve between the two monomers, with differences in absorption intensity. The 1Co/1Fe-CNT had the highest light absorption intensity of all the composites synthesized. The Kubelka-Munk function Tauc plot ($\alpha h\upsilon = A(h\upsilon-E_g)^n$) was employed to calculate the optical bandgap energy of the catalysts [43]. From Fig. 4b, the optical band gap values for $CoSe_2$, 2Co/1Fe-CNT, 1Co/1Fe, 1Co/1Fe-CNT, 1Co/2Fe-CNT and $FeSe_2$ were 1.26, 1.39, 1.41, 1.43, 1.52 and 1.63 eV, respectively. The above results illustrated that a
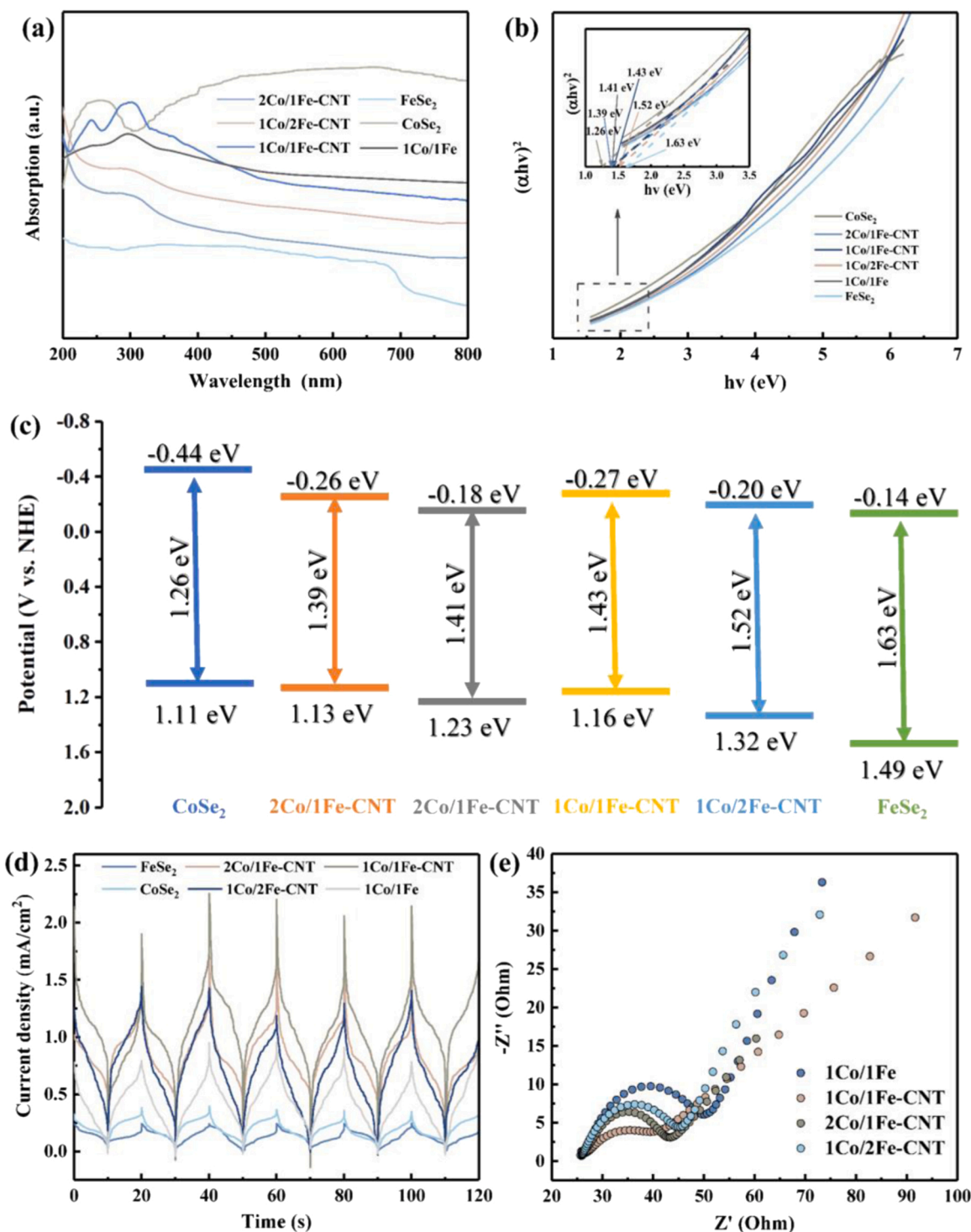

Fig. 4. (a) UV–vis DRS spectra of as-prepared catalysts. (b) Plots of $(\alpha h\upsilon)^2$ vs. $h\upsilon$ for the bandgap energies of the catalysts, and (c) their corresponding energy level band edge diagram of the Mott-Schottky plots. (d) Photocurrent curves and (e) EIS plots of as-prepared samples.

suitable ratio of Co to Fe source could enhance the light capture capability of the synthesized catalyst. Besides, the prepared catalysts were characterized for electrochemical properties by Mott-Schottky (M-S) analysis (Fig. S4). The M-S plots showed that the samples were all n-type semiconductors. The CB values of the catalysts were calculated by subjecting the flat band potentials obtained to a series of transformations [44]. The VB was obtained by summing the band gap energy with the CB value [45]. According to Fig. 4c, the complexation of CoSe$_2$ with FeSe$_2$ caused the E_{CB} and E_{VB} of the composites to move in the range of (-0.44 to -0.14 eV) and (1.11–1.49 eV), respectively. Due to the high CB (-0.14 V) and VB (1.49 V) of FeSe$_2$, the Fermi energy levels of the composites would be balanced and situated between the Fermi energy levels of the two monomers. With the increase of the Fe source, the bandwidth was shifted in the positive direction, which was caused by the flow of photoexcited carriers triggered by the built-in electric field generated at the heterogeneous interface [46].

To determine the efficiency of photogenerated charge separation and the lifetime of photoexcited carriers, the transient photocurrent response of the catalysts was analyzed in this work [47]. In Fig. 4d, the

photocurrent density of the composites was significantly higher than that of the two monomers, confirming that the construction of the heterojunction improved the separation and mobility of the photogenerated carriers. 1Co/1Fe-CNT had a significantly higher photocurrent density than the other samples, indicating that a suitable proportion of metal source could optimize the built-in electric field. Notably, the response intensity of 1Co/1Fe-CNT was about twice that of 1Co/1Fe, suggesting that the loading of CNTs could significantly improve the photoelectric properties of the composite [48]. The EIS Nyquist plot (Fig. 4e) corroborated the results of the transient photocurrent response, with the arcs ranked 1Co/1Fe > 1Co/2Fe-CNT > 2Co/1Fe-CNT > 1Co/1Fe-CNT. The 1Co/1Fe-CNT had the smallest arc diameter, indicating that the carriers encountered the least impedance during migration, thereby accelerating the photocatalytic reaction.

3.3. Catalytic Performance

The catalytic property of Co/Fe-CNT was assessed by PMS activation/photocatalysis for the removal of levofloxacin (LVF) (Fig. 5a). The
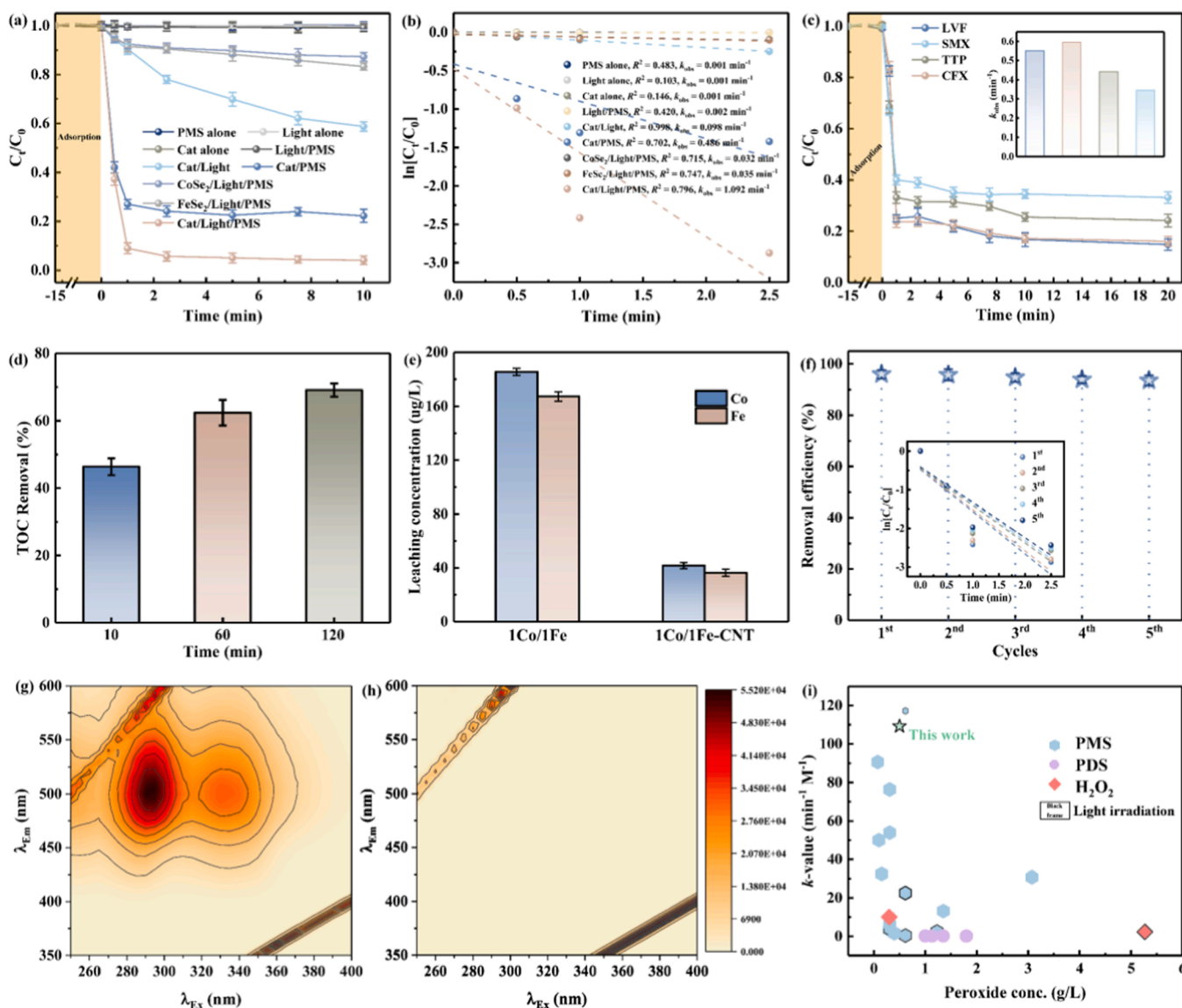
Fig. 5. (a) LVF degradation in various systems [Cat. = 1Co/1Fe-CNT], and (b) the corresponding pseudo-first-order kinetics. (c) Multi-pollutant degradation in 1Co/1Fe-CNT/PMS/light system, and (d) the corresponding TOC removal and (e) metal ion leaching. (f) LVF degradation in the 1Co/1Fe-CNT/PMS/light system during five cycles. 3D EEMs fluorescence spectra of the LVF solution at the catalytic system for (g) 0 min and (h) 2.5 min (i) Comparison of the k-values of LVF removal by various catalysts.

results of dark adsorption before light irradiation and PMS addition showed only 5.49 % of LVF was adsorbed by 1Co/1Fe-CNT within 60 min, which suggested negligible adsorption capacity of the prepared sample for LVF (Fig. S5). The control experiments excluded the degradation of LVF by PMS, light irradiation, and catalyst in the presence of the contaminant solution alone. In addition, the solely CoSe$_2$ and FeSe$_2$ could not effectively remove LVF (about 12.6 % and 16.7 % removal efficiency, respectively) within 10 min by photocatalysis coupled with PMS, while the composite 1Co/1Fe-CNT could remove 77.8 % of LVF within 10 min by activating PMS. The 1Co/1Fe-CNT also exhibited photocatalytic property, with a degradation efficiency of 41.2 % for LVF in the catalyst/light system. Significantly, the 1Co/1Fe-CNT/PMS/light system showed the highest LVF degradation efficiency of about 100 % and its reaction rate constant k_{obs} was more than twice that of the 1Co/1Fe-CNT/PMS system (Fig. 5b), which indicated that the light drove the internal electron transfer of the composite and played a synergistic role in boosting the LVF degradation [49]. Moreover, the effect of different Co/Fe sources and different catalytic conditions on the degradation of LVF was further explored (Figs. S6-S8).

To examine the practicality of 1Co/1Fe-CNT, simulated multi-polluted wastewater was employed for testing with 5 mg/L each of LVF, trimethoprim (TTP), ciprofloxacin (CFX) and sulfamethoxazole (SMX) added in solution. Fig. 5c showed that the 1Co/1Fe-CNT/PMS/light system could effectively remove most of the target pollutants within 20 min, and the degradation efficiency of all four pollutants exceeded 60 %, with LVF and CFX reaching more than 80 %. The result implied the potential application of 1Co/1Fe-CNT in advanced oxidation processes. The molecular structures of the four pollutants are different (Fig. S9), which might be the reason for their different degradation effects. The electrophile radicals prefer to interact with electron-donating groups, for example dialkyl amino (-NR$_2$), alkoxy (-OR) and amino (-NH$_2$). The slightly lower degradation efficiency of SMX might also be attributed to the high bond energy of the S=O bond.

Correspondingly, the TOC of the multi-pollutant model solution was measured after reaction (Fig. 5d). The pollutants were continuously degraded in the 1Co/1Fe-CNT/PMS/light system with TOC removal efficiencies of 46.3 %, 62.4 % and 69.1 % at 10 min, 60 min and 120 min, respectively, which showed a superior capability for the purification of multi-pollutant water. Fig. S10 showed the removal and mineralization capacity of the degradation system for the above pollutants individually. The removal rate constant k_{obs} for all four pollutants was above 0.3 min^{-1}, and the removal efficiency of TOC was also reached above 65 %. The application performance of 1Co/1Fe-CNT in more complex water matrices situations was also explored, including wide pH suitability and resistance to co-existing ions (Fig. S11 and Fig. S12). In general, the leaching of metal ions is one of the important factors for the stability of reaction catalysts, and the involvement of leached ions in catalytic reactions is the key to judge the catalyst performance [50]. Fig. 5e showed that the leaching of Co in 1Co/1Fe-CNT/PMS/light system was only 41.77 μg/L and Fe was 36.29 μg/L, which were much smaller than their leaching in the 1Co/1Fe/PMS/light system (Co: 185.42 μg/L, Fe: 167.28 μg/L), which suggested that the stability of the composite was enhanced by the addition of CNTs. Fig. S13 evaluated the possible contribution of leached ions Co^{2+} (42 μg/L) and Fe^{2+} (37 μg/L) to the catalytic reaction. It was clear that the homogeneous Co^{2+}/PMS/light and Fe^{2+}/PMS/light removed only about 4 % of LVF within 10 min, indicating that the contribution of leached Co and Fe in the reaction was insignificant. Meanwhile, the date presented in Fig. S14 indicated that the used 1Co/1Fe-CNT sample retained its original crystal structure, which demonstrated outstanding stability. Furthermore, 1Co/1Fe-CNT exhibited promising reusability (Fig. 5f). Although the rate constants k_{obs} decreased after 5 cycles (thumbnail), the catalyst maintained a high degradation property for LVF within 10 min
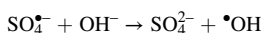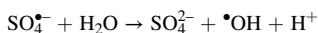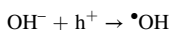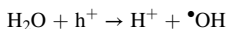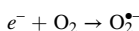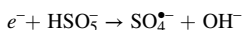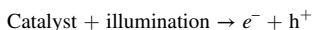
The 3D EEMs visually verified the degradation of LVF on the 1Co/1Fe-CNT/PMS/light system (Fig. 5g-h). In the control LVF solution,

two major peaks located at $E_x/E_m = (270-320)/(450-550)$ nm and $E_x/E_m = (320-350)/(460-540)$ nm were attributed to humic acid, which was detected due to its conjugated heterocyclic structure [51]. After 2.5 min of catalytic reaction by the 1Co/1Fe-CNT/PMS/light system, the peaks disappeared, which demonstrated the destruction of the conjugated heterocyclic structure of LVF and the breakdown of the LVF molecules in solution into smaller molecules. A variety of heterogeneous Fenton-like systems for LVF removal were compared in Fig. 5i and Table S1. Considering the effect of reaction conditions on k_{obs}, a normalized kinetic model (k-value is k_{obs} divided by catalyst dosage and oxidant concentration, and multiplied by pollutant concentration) was introduced to evaluate the reaction rates of these heterogeneous Fenton-like systems [52]. It was obtained from the figure that the k-value of 1Co/1Fe-CNT exceeded the most catalyst samples reported for Fenton-like reactions towards LVF removal.

3.4. Determination of ROS

Since the adsorption of LVF by the catalyst was negligible, the rapid removal of LVF was due to the catalytic oxidation process [53]. The relevant ROS in the 1Co/1Fe-CNT/PMS/light system were investigated by employing EPR measurements. 5,5-dimethyl-1-pyrroline-N-oxide (DMPO) and 2,2,6,6-tetramethyl-4-piperidine (TEMP) were chosen as free radicals (sulfate radical (SO$_4^{\bullet-}$), hydroxyl radical ($^{\bullet}$OH) and superoxide radical (O$_2^{\bullet-}$)) and singlet oxygen (^{1}O$_2$) trappers. As shown in Fig. S15a, in the presence of PMS solely, only a little SO$_4^{\bullet-}$ and $^{\bullet}$OH were produced. When the catalyst was added, PMS was rapidly activated and decomposed into SO$_4^{\bullet-}$ and $^{\bullet}$OH, and the free radical content in the solution increased with time. The activation by the catalysts with different Co, Fe source ratios for PMS was different (Fig. S15b), which further indicated that a suitable metal source ratio could optimize the electron transfer rate and improved the catalytic performance. Similarly, O$_2^{\bullet-}$ was captured at 1 min of the catalytic reaction (Fig. S15c), demonstrating that a photocatalytic reaction accompanied the LVF degradation process. However, when ^{1}O$_2$ was captured using TEMP, no characteristic signal was detected. Therefore, there might be no involvement of ^{1}O$_2$ in the 1Co/1Fe-CNT/PMS/light system. The contribution of ROS to LVF elimination was further verified by chemical quenching experiments (Fig. S16). The inhibition of LVF degradation by the quenchers was ranked as Meth > TBA > p-BQ > Na$_2$C$_2$O$_4$ > L-histidine > FFA, indicating that SO$_4^{\bullet-}$ and $^{\bullet}$OH were the main ROS in the 1Co/1Fe-CNT/PMS/light system. Subsequently, the inhibition by p-BQ and Na$_2$C$_2$O$_4$ followed, which suggested that O$_2^{\bullet-}$ and h$^+$ contributed to the reaction to a minor degree. The charge transfer in the 1Co/1Fe-CNT was consistent with the characteristic displayed by heterojunction, which inhibited the recombination of electron-hole pairs and contributed to the transfer of photogenerated electrons. The impact of FFA and L-histidine on LVF degradation was negligible, further indicating that ^{1}O$_2$ was not involved in the reaction. It was noteworthy that the degradation k_{obs} in the reaction solution with addition of L-histidine was slightly lower than that with addition of FFA, which was caused by the direct reaction of L-histidine with PMS in the solution and the depletion of PMS content (Fig. S17), thus slowing down the degradation rate of LVF [54].

Taken together, the mechanisms underlying the evolution of active species in the SR-photo system could be summarized as follows. The catalyst was excited by light irradiation to produce electrons and holes (Eq. 1). The heterogeneous structure drove the internal electric field to be exploited. Subsequently, the electrons reacted with PMS to form SO$_4^{\bullet-}$ and also with O$_2$ to produce O$_2^{\bullet-}$ (Eqs. 2–3). Meanwhile, the holes reacted with water molecules or hydroxyl to generate $^{\bullet}$OH (Eqs. 4–5). On the other hand, the redox cycle between the transition metals could drive the production of SO$_4^{\bullet-}$ (Eqs. 6–7), which further promoted the formation of $^{\bullet}$OH (Eqs. 8–9). In summary, the synergistic effect of PMS activation and photocatalysis results in the rapid degradation of the pollutant with SO$_4^{\bullet-}$ and $^{\bullet}$OH as the dominant active species.

$$Catalyst + illumination \rightarrow e^- + h^+ \tag{1}$$

$$e^- + HSO_5^- \rightarrow SO_4^{\bullet-} + OH^- \tag{2}$$

$$e^- + O_2 \rightarrow O_2^{\bullet-} \tag{3}$$

$$H_2O + h^+ \rightarrow H^+ + {}^{\bullet}OH \tag{4}$$

$$OH^- + h^+ \rightarrow {}^{\bullet}OH \tag{5}$$

$$M^{n+} (M = Co\ or\ Fe) + HSO_5^- \rightarrow M^{(n+1)+} + SO_4^{\bullet-} + OH^- \tag{6}$$

$$M^{(n+1)+} (M = Co\ or\ Fe) + HSO_5^- \rightarrow M^{n+} + SO_5^{\bullet-} + H^+ \tag{7}$$

$$SO_4^{\bullet-} + H_2O \rightarrow SO_4^{2-} + {}^{\bullet}OH + H^+ \tag{8}$$

$$SO_4^{\bullet-} + OH^- \rightarrow SO_4^{2-} + {}^{\bullet}OH \tag{9}$$

3.5. Investigation of interfacial interactions

Density functional theory (DFT) calculations provided insight into the fundamental mechanism of the high catalytic activity of catalyst in this work. Based on the information from Fig. S18, it could be seen that the work functions of $CoSe_2$ and $FeSe_2$ were 4.217 eV and 4.354 eV, respectively, indicating that $CoSe_2$ had a high Fermi energy level. Accordingly, the energy band structures of $CoSe_2$ and $FeSe_2$ heterostructure could be proposed (Fig. 6). When the heterostructure was constructed, the accumulated electrons in the Fermi energy level of $CoSe_2$ would migrate to the Fermi energy level of $FeSe_2$ until the equilibrium of the two Fermi energy levels was achieved, which induced the internal electric field at the interface [55]. During illumination, the photogenerated electron and holes (e^--h^+) pairs were generated, and the bending of the energy bands during the alignment of the Fermi energy levels drove a lower CB potential in $FeSe_2$ and a lower VB potential in $CoSe_2$ than before, leading to easier transfer of photogenerated electrons from $FeSe_2$ to $CoSe_2$ and combined with holes in $CoSe_2$ [56]. Meanwhile, e^- on CB of $CoSe_2$ would reduce O_2 to $O_2^{\bullet-}$.

The interfacial interactions of the prepared catalyst were also explored. As shown in Fig. 7a, when the heterojunction structure was realized, the band gap showed a shift near the Fermi energy level, and the increase of total density of states (TDOS) of the heterostructure implied a stronger electron transfer compared to sole $FeSe_2$ and $CoSe_2$. The TDOS of $FeSe_2$-CNT and $CoSe_2$-CNT was also investigated (Fig. 7b).

Apparently, the introduction of CNTs promoted the increase of TDOS of $CoSe_2$ and $FeSe_2$, which proved that CNTs facilitated the electron transfer efficiency of monomeric $CoSe_2$ and $FeSe_2$. Therefore, the synergistic interaction of the multiphase interface with the carbon substance could excite more electron activity [57]. Fig. 7c showed the schematic illustration of electron transfer in the contact between $CoSe_2$ and $FeSe_2$. As $CoSe_2$ and $FeSe_2$ came into contact with each other, the electrons in $CoSe_2$ were transferred to $FeSe_2$ due to the difference in Fermi energy levels. During the reaction, owing to the existence of electric field within the heterogeneous interface, electrons converged on the surface of $FeSe_2$.

For the purpose of further understanding of the improvement in catalytic performance, a simplified model of the different interfaces was developed and the corresponding difference charge densities were presented. From Fig. 7d and g, the cell parameters of $CoSe_2$ and $FeSe_2$ were similar, and the surface lattices of both components were well-matched. After the optimization of structure, the strong interaction was generated between $CoSe_2$ and $FeSe_2$ at the interface, and the interfacial electrons of $CoSe_2$ were transferred to $FeSe_2$, which suggested that the catalytic performance of the catalyst could be enhanced by the coupling effect in the heterogeneous interface, where electron transfer could be effectively facilitated [58]. Fig. 7e, f, h, i showed the difference charge density of CNTs bound to $CoSe_2$ and $FeSe_2$, respectively. From Fig. 7 f and g, it could be seen that the formation of CNT-$CoSe_2$ interface was accompanied by the transfer of active electrons from CNTs to $CoSe_2$, and the similar interactions between $FeSe_2$ and CNTs were observed (Fig. 7 h and i). Based on the analysis of DFT calculations, it was proved that an electron transfer bridge could be formed by the robust interaction between $FeSe_2$ and $CoSe_2$, which was more facilitative for electron transport than the monomer. The rational design of Co/Fe-CNT had excellent catalytic performance and had great potential for applications in the field of efficient catalysis.

The adsorption model for PMS was further analyzed by applying DFT. The adsorption of PMS on the exposed surfaces of both monomers was displayed in Fig. 8a, b. The adsorption energies (ΔE_{ads}) of $CoSe_2$ and $FeSe_2$ on PMS were -1.35 eV and -1.10 eV, respectively, suggesting that PMS had great adsorption capacity on both substrates. Compared to a pure PMS molecule ($l_{O-O} = 1.399$ Å) (Fig. S19), the O_α-O_β bond elongated with l_{O-O} of 1.468 Å and 1.459 Å for $CoSe_2$-PMS and $FeSe_2$-PMS, where the O_β atom bonded to a metal atom on the catalyst surface. This result indicated that the metal-element-containing catalysts favored decomposition of PMS and generation of radicals. Fig. 8c, f and Fig. S20
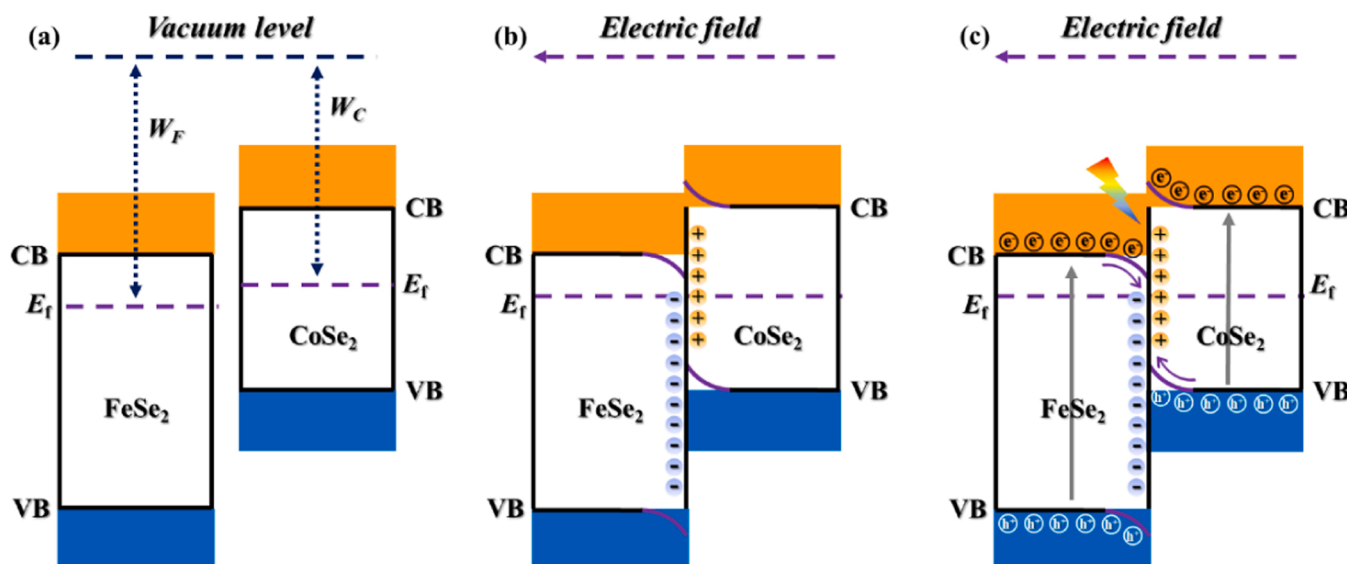

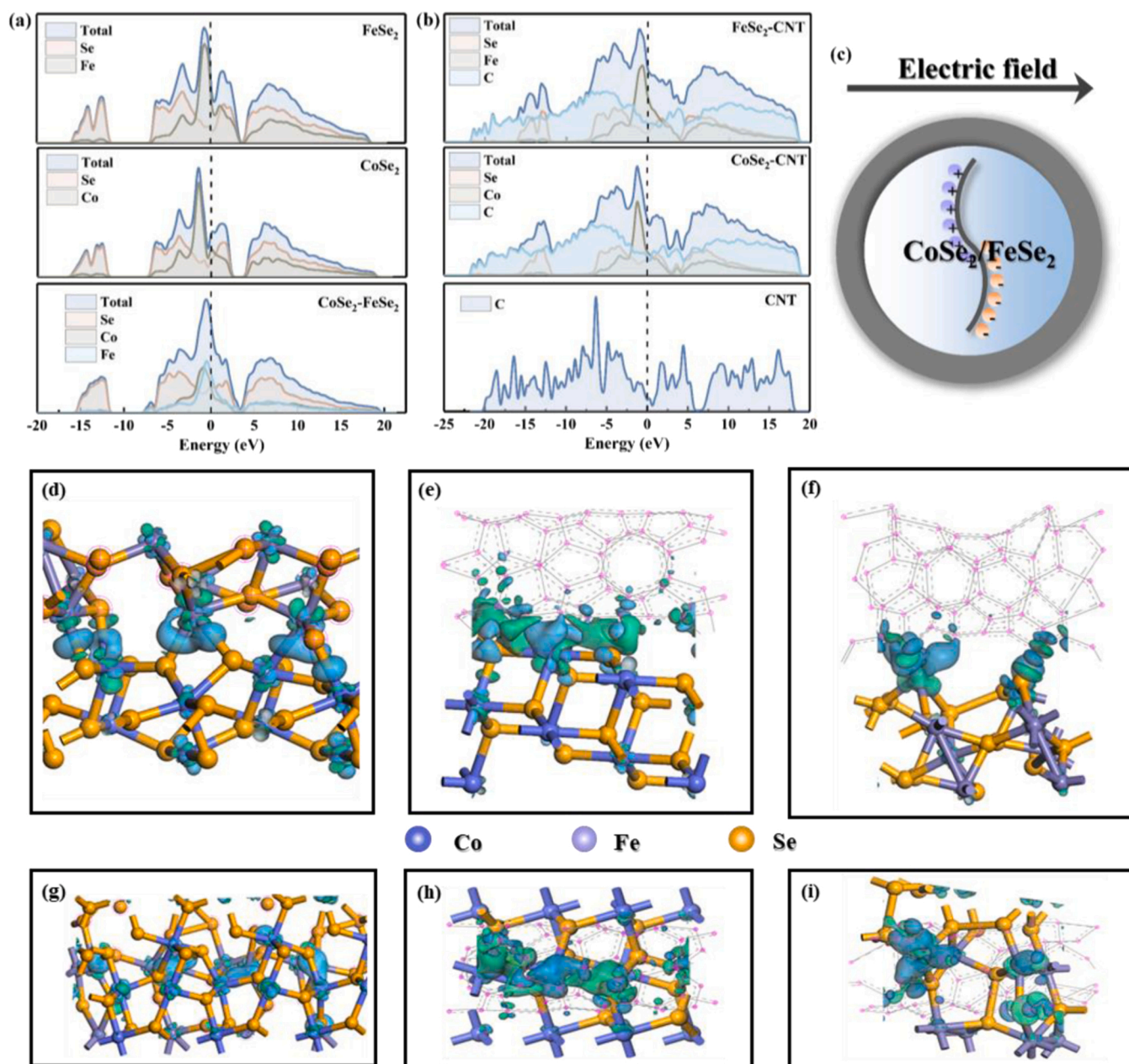**Fig. 6.** The heterojunction charge transfer process.

Fig. 7. (a,b) Calculated TDOS analyses. (c) Schematic of the electron transfer between $CoSe_2$ and $FeSe_2$. Charge density difference for $CoSe_2/FeSe_2$, $FeSe_2$-CNT and $CoSe_2$-CNT from side (d-f) and top (g-i) views, the aggregation and dissipation of electrons are represented by the blue and green isosurfaces.

exhibited the difference charge density of PMS adsorbed by $FeSe_2$ with Se vacancies ($FeSe_2$–V_{Se}). The more concentrated positive and negative isosurfaces were enriched at the adsorption bonds and the adsorption energy was higher ($\Delta E_{ads} = -3.68$ eV), which implied that the formation of Se vacancies made the catalyst surface easier to adsorb PMS. The greater adsorption energy between two interfaces suggested that the peroxide bond of PMS was more susceptible to form $SO_4^{\bullet-}$ radicals on the surface of $FeSe_2$–V_{Se} by electron transition [59].

To further examine the superior adsorption property of Se vacancy containing surface after the formation of heterojunction for PMS, the interaction between PMS and metal center on different surfaces was analyzed using the crystal orbital Hamilton population (COHP) [60]. In the COHP plot (Fig. 8g), the red area (right side) represented the bonding contribution and the blue area (left side) represented the antibonding contribution. It was observed that the bonding state occupancy of Fe-PMS in $FeSe_2$–V_{Se} was higher than that of $CoSe_2$ and $FeSe_2$,

indicating improved Fe-PMS interactions for PMS in the $FeSe_2$–V_{Se} model. Moreover, the values of integrated COHP (ICOHP), which quantitatively characterized the bonding strength, were calculated. When adsorbed PMS interacted with surface Fe atoms in $FeSe_2$ containing Se vacancies, the vacancy sites could assist to facilitate the bonding of O_β in the PMS molecule to the surface Fe atoms, which in turn accelerated the decomposition of PMS and boosted the generation of radicals. The ICOHP values on $FeSe_2$ and $FeSe_2$–V_{Se} were − 0.17 and -0.74 (Table S2), respectively, indicating that the formation of surface vacancy sites significantly increased the interaction between PMS and the metal sites. In summary, the construction of the $CoSe_2$-$FeSe_2$ heterojunction resulted in the formation of Se vacancies on the exposed surface, enhancing the interaction between the PMS and the active site and promoting its charge transfer, which led to superior activation activity of the composite towards the PMS.
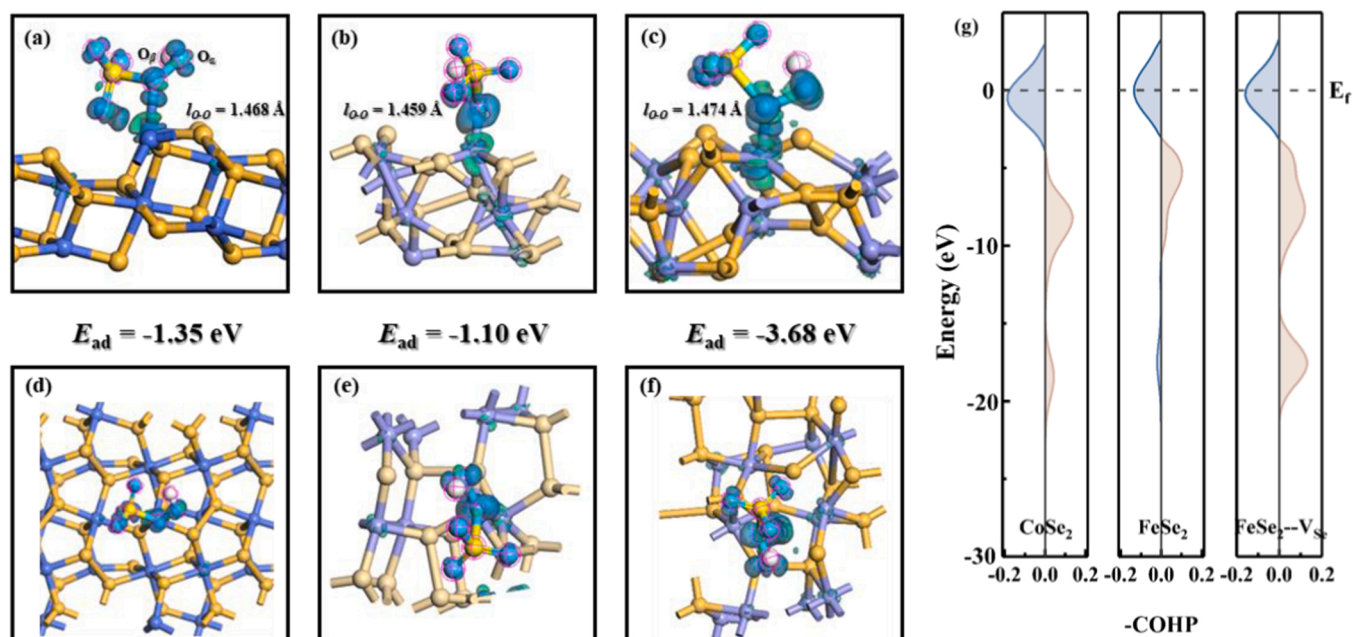
Fig. 8. DFT calculation models (difference charge density) showing the adsorption of PMS onto (a) CoSe$_2$, (b) FeSe$_2$ and (c) FeSe$_2$–V$_{Se}$ in side view and (d-f) top view, the aggregation and dissipation of electrons are represented by the blue and green isosurfaces. (g) Calculated COHP between the metal center and PMS.

3.6. Degradation pathways and toxicity prediction

The molecular structure of LVF (Fig. 9a and Fig. S21) was analyzed using Conceptual Density Functional Theory (CDFT) calculations. It was shown in the HOMO orbitals (Fig. 9b) that the electron-rich regions were primarily situated in the 1 C, 9 N, 2 C, 10 C and 21 O areas, while the LUMO orbital (Fig. 9c) indicated the location of the concentration for the more electronegative atoms, on 4 C, 27 N, 35 C, 38 O and 40 O,
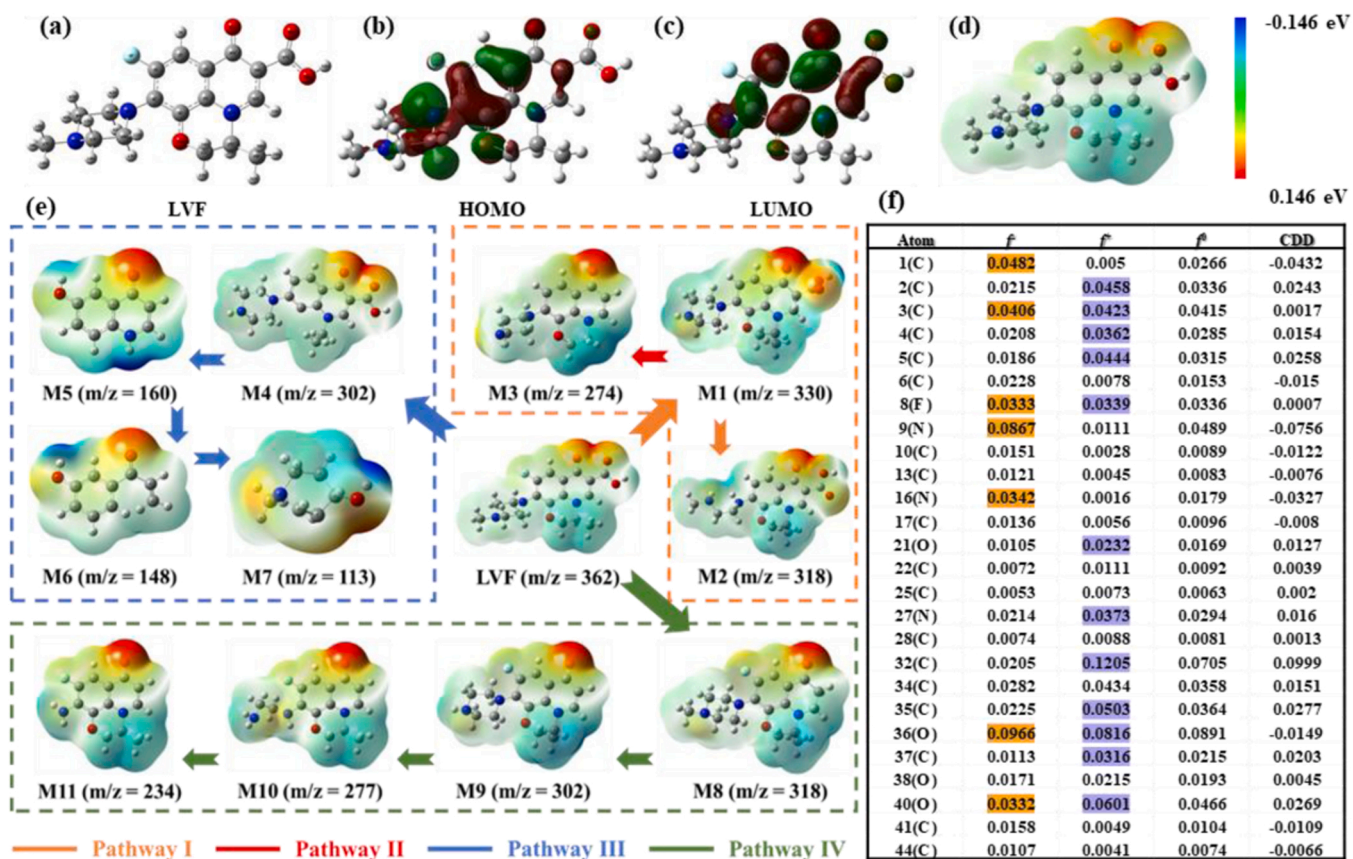

Atom	f^-	f^+	f^0	CDD
1(C)	0.0482	0.005	0.0266	-0.0432
2(C)	0.0215	0.0458	0.0336	0.0243
3(C)	0.0406	0.0423	0.0415	0.0017
4(C)	0.0208	0.0362	0.0285	0.0154
5(C)	0.0186	0.0444	0.0315	0.0258
6(C)	0.0228	0.0078	0.0153	-0.015
8(F)	0.0333	0.0339	0.0336	0.0007
9(N)	0.0867	0.0111	0.0489	-0.0756
10(C)	0.0151	0.0028	0.0089	-0.0122
13(C)	0.0121	0.0045	0.0083	-0.0076
16(N)	0.0342	0.0016	0.0179	-0.0327
17(C)	0.0136	0.0056	0.0096	-0.008
21(O)	0.0105	0.0232	0.0169	0.0127
22(C)	0.0072	0.0111	0.0092	0.0039
25(C)	0.0053	0.0073	0.0063	0.002
27(N)	0.0214	0.0373	0.0294	0.016
28(C)	0.0074	0.0088	0.0081	0.0013
32(C)	0.0205	0.1205	0.0705	0.0999
34(C)	0.0282	0.0434	0.0358	0.0151
35(C)	0.0225	0.0503	0.0364	0.0277
36(O)	0.0966	0.0816	0.0891	-0.0149
37(C)	0.0113	0.0316	0.0215	0.0203
38(O)	0.0171	0.0215	0.0193	0.0045
40(O)	0.0332	0.0601	0.0466	0.0269
41(C)	0.0158	0.0049	0.0104	-0.0109
44(C)	0.0107	0.0041	0.0074	-0.0066

Fig. 9. (a) Optimized structure of LVF. Schematic of (b) HOMO, (c) LUMO and (d) ESP for LVF. (e) Possible degradation pathways of LVF. (f) Fukui index (f^-, f^+ and f^0) of LVF.

respectively. The ESP map of the LVF reflected the distribution of the surface electron cloud (Fig. 9d), which allowed visualizing the state of the LVF molecular electron distribution. By the aggregation and distribution of electrons on LVF molecular, the vulnerable area could be tentatively determined to be located in the electron-rich region and the negatively charged region. Moreover, the Fukui index was shown in Fig. 9f. It was possible to identify the reaction sites of the active component on LVF molecules from the specific indices (f^+, f^-, f^0 and CDD). The sites with higher values of f^+, f^- and f^0 were more sensitive to attack by the active species during the reaction [61]. Specifically, $SO_4^{\bullet-}$ and $O_2^{\bullet-}$ tended to attack the higher f^+ sites as nucleophilic species, while $^{\bullet}OH$ or h^+ as electrophilic species preferred to destroy the higher f^- sites. The CDD index, which represented the location of the distribution for nucleophilic and electrophilic sites, showed that ring chains with N atoms and sites with O-atom functional groups could be easily attacked, allowing LVF to be broken down into smaller molecules.

Liquid chromatography tandem mass spectrometry (LC-MS/MS) was employed to detect the intermediates produced during the LVF degradation (Fig. S22). Since LVF molecule has a variety of electron-rich groups, including C-C double bonds, carboxyl groups, and carbonyl groups, it is susceptible to be attacked by radicals and undergoes electrophilic reactions. The degradation pathways of LVF included decarboxylation, defluorination, demethylation, decarbonylation, and cleavage of C-N bonds (Fig. 9e). At first, LVF underwent demethylation and defluorination to form M1, which was susceptible to be attacked by $^{\bullet}OH$ and $SO_4^{\bullet-}$ for C-N bond cleavage and decarboxylated to form M2 and M3. Due to the high f^+ of 21 O, LVF was also vulnerable to degradation by $SO_4^{\bullet-}$ and $O_2^{\bullet-}$ attack to form M4. In the presence of multiple ROS, M4 underwent decarboxylation, demethylation and C-N cleavage to produce M5, which in turn continued to be oxidized to M6 and M7. The electronegativity of 38 O and 40 O was relatively high, thus LVF might also suffer from decarboxylation to generate M8, followed by demethylation (M9) and gradual C-N cleavage, and further degraded to lower molecular masses M10 and M11. The oxidation intermediates were then completely mineralized to inorganic substances CO_2, H_2O and NO_3^-.

Based on the exposed functional groups of intermediates obtained from the above analysis, both acute toxicity and chronic toxicity of LVF and the degradation intermediates were assessed using ECOSAR software (Fig. 10a). In general, most of the intermediates, such as M1, M2,

M4, M5, M7 and M11, had no acute or chronic toxicity. For the prediction of acute toxicity, all intermediates were not toxic to fish and dolphins, only M8 was toxic to green algae. In addition, both the medium molecule M3 and the small molecule M6 were chronically toxic, in which the toxicity of M6 might be attributed to the carbonyl group linking the double bond of carbon. Moreover, chronic toxicity of M8, M9 and M10 was increased due to the destruction of the hydrophilic group (carboxyl group) first. As predicted by the Biowin model (Fig. 10b), LVF was classified as a less biodegradable compound, and most of its degradation intermediates also demonstrated difficult biodegradability. Therefore, control of the degradation pathway is necessary, for instance, decarboxylation steps should be eschewed as far as possible to expose the more toxic groups (aniline, vinyl/allyl, etc.). Meanwhile, the toxicity and difficult biodegradability of intermediates can be greatly reduced by accelerating the rate of degradation and enhancing the efficiency of mineralization.

4. Conclusion

In summary, V_{Se}-vacancy-rich engineered Co/Fe-CNT catalyst with carbon nanotubes loading was prepared using selenization and hydrothermal processes to degrade antibiotics through photocatalysis synergistic PMS activation (SR-photo system). The construction of interfacial heterojunctions led to the formation of built-in electric fields within the catalyst, significantly enhancing photocatalytic performance. And the CNTs loading accelerated the electron transfer rate at the interface. Experimental results showed that the 1Co/1Fe-CNTs exhibited excellent degradation of contaminants in the SR-photo system, with outstanding stability and durability. Complete removal of LVF was achieved within 10 min, and the mineralization efficiency was as high as 65 % in multipollutants matrix within 120 min. The metal leaching from the catalyst remained at a low level even after reuse. Systematic electrochemical measurements determined the direction of charge flow under illumination, and DFT calculational analysis revealed that the $CoSe_2/FeSe_2$ heterojunctions modulated the surface electronic structure and local coordination environment. The introduction of V_{Se} promoted the redox cycle of transition metals within the catalyst, enhancing the adsorption energy of PMS on the catalyst surface, and boosting the production of reactive oxygen species. Furthermore, degradation pathways and
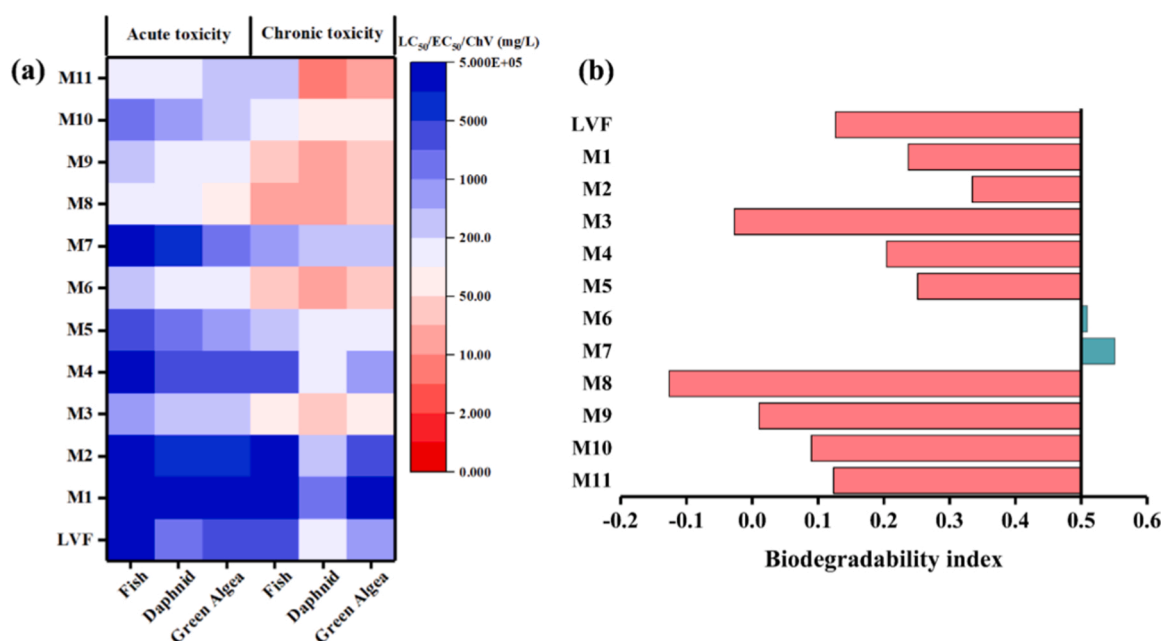

Fig. 10. (a) Predicted acute and chronic toxicity of LVF and its degradation intermediates. (b) Biodegradability of LVF and intermediates predicted using Biowin model.

toxicity prediction of intermediates were presented. Overall, the results of this work provide guidelines for the design of high-performance environmental catalytic materials for defect engineering and broaden the application of transition metal selenides in the environmental field.

CRediT authorship contribution statement

Yuxuan He: Investigation, Resources, Formal analysis, Writing – original draft, Visualization. **Jin Qian:** Conceptualization, Writing – review & editing, Supervision, Funding acquisition. **Peifang Wang:** Conceptualization, Supervision. **Taiping Xie:** Conceptualization, Supervision. **Dionysios D. Dionysiou:** Writing – review & editing, Supervision. **Bianhe Lu:** Validation, Investigation. **Sijing, Tang:** Validation, Investigation.

Declaration of Competing Interest

The authors declare that they have no known competing financial interests or personal relationships that could have appeared to influence the work reported in this paper.

Data availability

Data will be made available on request.

Acknowledgement

Appendix A. Supporting information

Supplementary data associated with this article can be found in the online version at doi:10.1016/j.apcatb.2023.122620.

References

[1] Z. Lin, T. Yuan, L. Zhou, S. Cheng, Xu Qu, P. Lu, Q. Feng, Impact factors of the accumulation, migration and spread of antibiotic resistance in the environment, Environ. Geochem. Health 43 (5) (2021) 1741–1758.

[2] E.Y. Klein, T.P. Van Boeckel, E.M. Martinez, S. Pant, S. Gandra, S.A. Levin, H. Goossens, R. Laxminarayan, Global increase and geographic convergence in antibiotic consumption between 2000 and 2015, PNAS 115 (15) (2018) 3463–3470.

[3] J. Lim, M.R. Hoffmann, Peroxymonosulfate (PMS) activation on cobalt-doped TiO2 nanotubes: degradation of organics under dark and solar light irradiation conditions, Environ. Sci. Nano 7 (2020) 1602–1611.

[4] L. Ling, D. Zhang, C. Fan, C. Shang, A. Fe, II)/citrate/UV/PMS process for carbamazepine degradation at a very low Fe (II)/PMS ratio and neutral pH: the mechanisms, Water Res. 124 (2017) 446–453.

[5] G. Farshid, M. Mahsa, Application of peroxymonosulfate and its activation methods for degradation of environmental organic pollutants: review, Chem. Eng. J. 310 (2017) 41–62.

[6] W. Han, D. Li, M. Zhang, H. Ximin, X. Duan, S. Liu, S. Wang, Photocatalytic activation of peroxymonosulfate by surface-tailored carbon quantum dots, J. Hazard. Mater. 395 (2020), 122695.

[7] H. Guo, H.Y. Niu, C. Liang, C.G. Niu, Y. Liu, N. Tang, Y. Yang, H.Y. Liu, Y.Y. Yang, W.J. Wang, Few-layer graphitic carbon nitride nanosheet with controllable functionalization as an effective metal-free activator for peroxymonosulfate photocatalytic activation: role of the energy band bending, Chem. Eng. J. 401 (2020), 126072.

[8] J. Zhang, C. Zhai, W. Zhao, Y. Chen, R. Yin, L. Zeng, M. Zhu, Insight into combining visible-light photocatalysis with transformation of dual metal ions for enhancing peroxymonosulfate activation over dibismuth copper oxide, Chem. Eng. J. 390 (2020), 124582.

[9] J. Zhang, W. Zhao, Z. Li, G. Lu, M. Zhu, Visible-light-assisted peroxymonosulfate activation over Fe (II)/V(IV) self-doped FeVO4 nanobelts with enhanced sulfamethoxazole degradation: performance and mechanism, Chem. Eng. J. 403 (2021), 126384.

[10] Z.M. Gao, J.Z. Zhu, Q.Z. Zhu, C.S. Wang, Y.Y. Cao, Spinel ferrites materials for sulfate radical-based advanced oxidation process: a review, Sci. Total. Environ. 847 (15) (2022), 157405.

[11] S. Bai, L. Wang, Z.Q. Li, Y.J. Xiong, Facet-engineered surface and interface design of photocatalytic materials, Adv. Sci. 4 (2017), 1600216.

[12] J. Li, Y. Li, Z. Xiong, G. Yao, B. Lai, The electrochemical advanced oxidation processes coupling of oxidants for organic pollutants degradation: a mini-review, Chin. Chem. Lett. 30 (2019) 2139–2146.

[13] R. Xiao, Z. Luo, Z. Wei, S. Luo, R. Spinney, W. Yang, D.D. Dionysiou, Activation of peroxymonosulfate/persulfate by nanomaterials for sulfate radical-based advanced oxidation technologies, Curr. Opin. Chem. Eng. 19 (2018) 51–58.

[14] L. Zhu, J. Ji, J. Liu, S. Mine, M. Matsuoka, J. Zhang, M. Xing, Designing 3D-MoS2 sponge as excellent cocatalysts in advanced oxidation processes for pollutant control, Angew. Chem. Int. Ed. 33 (2020) 13968–13976.

[15] S.N.R. Inturi, M. Suidan, P.G. Smirniotis, Influence of synthesis method on leaching of the Cr-TiO2 catalyst for visible light liquid phase photocatalysis and their stability, Appl. Catal. B Environ. 180 (2016) 351–361.

[16] P.D. Hu, H.R. Su, Z.Y. Chen, C.Y. Yu, Q.L. Li, B.X. Zhou, P.J.J. Alvarez, M.C. Long, Selective degradation of organic pollutants using an efficient metal free catalyst derived from carbonized polypyrrole via peroxymonosulfate activation, Environ. Sci. Technol. 51 (2017) 11288–11296.

[17] F.P. Zhao, S.D. Shen, L. Cheng, L. Ma, J.H. Zhou, H.L. Ye, N. Han, T.P. Wu, Y.G. Li, J. Lu, Improved sodium-ion storage performance of ultrasmall iron selenide nanoparticles, Nano. Lett. 17 (2017) 4137–4142.

[18] R. Gao, H. Zhang, D.P. Yan, Iron diselenide nanoplatelets: stable and efficient water-electrolysis catalysts, Nano Energy 31 (2017) 90–95.

[19] C. Panda, P.W. Menezes, C. Walter, S.L. Yao, M.E. Miehlich, V. Gutkin, K. Meyer, M. Driess, From a molecular 2Fe-2Se precursor to a highly efficient iron diselenide electrocatalyst for overall water splitting, Angew. Chem., Int. Ed. 56 (2017) 10506–10510.

[20] G. Fang, T. Zhang, H. Cui, D.D. Dionysiou, C. Liu, J. Gao, Y.J. Wang, D.M. Zhou, Synergy between iron and selenide on FeSe2(111) surface driving peroxymonosulfate activation for efficient degradation of pollutants, Environ. Sci. Technol. 54 (23) (2020) 15489–15498.

[21] F. Chen, D. Shi, M. Yang, H. Jiang, Y. Shao, S. Wang, B. Zhang, J. Shen, Y. Wu, X. Hao, Novel designed MnS-MoS2 heterostructure for fast and stable Li/Na storage:insights into the advanced mechanism attributed to phase engineering, Adv. Funct. Mater. 31 (2021), 2007132.

[22] L. Cao, X. Liang, X. Ou, X. Yang, Y. Li, C. Yang, Z. Lin, M. Liu, Heterointerface engineering of hierarchical Bi2S3/MoS2 with self-generated rich phase boundaries for superior sodium storage performance, Adv. Funct. Mater. 30 (2020), 1910732.

[23] H. Shan, J. Qin, Y. Ding, H. Sari, X. Song, W. Liu, Y. Hao, J. Wang, C. Xie, J. Zhang, X. Li, Controllable heterojunctions with a semicoherent phase boundary boosting the potassium storage of CoSe/FeSe2, Adv. Mater. 33 (2021), 2170288.

[24] Y. Liu, H. Cheng, M. Lyu, S. Fan, Q. Liu, W. Zhang, Y. Zhi, C. Wang, C. Xiao, S. Wei, B. Ye, Yi Xie, Low overpotential in vacancy-rich ultrathin CoSe2 nanosheets for water oxidation, J. Am. Chem. Soc. 136 (44) (2014) 15670–15675.

[25] X.L. Zhang, S.J. Hu, Y.R. Zheng, R. Wu, F.Y. Gao, P.P. Yang, Z.Z. Niu, C. Gu, X. Yu, X.S. Zheng, C. Ma, X. Zheng, J.F. Zhu, M.R. Gao, S.H. Yu, Polymorphic cobalt diselenide as extremely stable electrocatalyst in acidic media via a phase-mixing strategy, Nat. Commun. 10 (1) (2019).

[26] B. Wang, K. Srinivas, X. Wang, Z. Su, B. Yu, Y. Liu, F. Ma, D.X. Yang, Y.F. Chen, Self-assembled CoSe2-FeSe2 heteronanoparticles along the carbon nanotube network for boosted oxygen evolution reaction, Nanoscale 13 (2021) 9651–9658.

[27] Z. Wu, G. Liang, J. Wu, W. Peng, F. Yang, L. Chen, B. Johannessen, Z. Guo, Synchrotron X-ray absorption spectroscopy and electrochemical study of Bi2O2Se electrode for lithium-/potassium-ion storage, Adv. Energy Mater. 11 (2021), 2100185.

[28] C. Kim, J.W. Jung, K.R. Yoon, D.Y. Youn, S. Park, I.D. Kim, A high-capacity and long-cycle-life lithium-ion battery anode architecture: silver nanoparticle-decorated SnO2/NiO nanotubes, ACS Nano 10 (2016) 11317.

[29] M. Yousaf, Z. Wang, Y. Wang, Y. Chen, U. Ali, M. Maqbool, A. Imran, N. Mahmood, P. Gao, R. Han, Core–shell FeSe2/C nanostructures embedded in a carbon framework as a free standing anode for a sodium ion battery, Small 16 (2020), 2002200.

[30] J. Ge, B. Wang, J. Wang, Q. Zhang, B. Lu, Nature of FeSe2/N-C anode for high performance potassium ion hybrid capacitor, Adv. Energy Mater. 10 (2019), 1903277.

[31] K. Srinivas, Y. Chen, B. Wang, B. Yu, Y. Lu, Z. Su, W.L. Zhang, D.X. Yang, Metal-organic framework-derived Fe-doped Ni3Fe/NiFe2O4 heteronanoparticle-decorated carbon nanotube network as a highly efficient and durable bifunctional electrocatalyst, ACS Appl. Mater. Interfaces 12 (2020) 55782–55794.

[32] B. Jia, Z. Xue, Q. Liu, Q. Liu, K. Liu, M. Liu, Hierarchical nanotubes constructed from CoSe2 nanorods with an oxygen-rich surface for an efficient oxygen evolution reaction, J. Mater. Chem. A 7 (2019) 15073–15078.

[33] L. Zhang, J. Liang, L. Yue, Z. Xu, K. Dong, Q. Liu, Y. Luo, T.S. Li, X.H. Cheng, G. W. Cui, B. Tang, A.A. Alshehri, K.A. Alzahrani, X.D. Guo, X.P. Sun, N-doped carbon nanotubes supported CoSe2 nanoparticles: A highly efficient and stable catalyst for H2O2 electrosynthesis in acidic media, Nano. Res. 15 (2022) 304–309.

[34] J. Kim, D. Hyun, K. Kawashima, J. Lin, H. Lim, An active nanoporous Ni (Fe) OER electrocatalyst via selective dissolution of Cd in alkaline media, Appl. Catal. B Environ. 225 (2018) 1–7.

[35] D. Zhao, R. Zhao, S. Dong, X. Miao, Z. Zhang, C. Wang, L. Yin, Alkali-induced 3D crinkled porous Ti_3C_2 MXene architectures coupled with NiCoP bimetallic phosphide nanoparticles as anodes for high-performance sodium-ion batteries, Energy Environ. Sci. 8 (2019) 2422–2432.

[36] H. Tabassum, C. Zhi, T. Hussain, T. Qiu, W. Aftab, R. Zou, Encapsulating trogtalite $CoSe_2$ nanobuds into BCN nanotubes as high storage capacity sodium ion battery anodes, Adv. Energy Mater. 9 (2019), 1901778.

[37] Q. Pan, M. Zhang, L. Zhang, Y. Li, Y. Li, C. Tan, F. Zheng, Y. Huang, H. Wang, Q. Li, $FeSe_2$@C microrods as a superior long-life and high-rate anode for sodium ion batteries, ACS Nano 14 (2020) 17683–17692.

[38] S. Lu, H. Wu, S. Xu, Y. Wang, J. Zhao, Y. Li, A. Abdelkader, J. Li, W. Wang, K. Xi, Y. Guo, S. Ding, G. Gao, R. Kumar, Iron selenide microcapsules as universal conversion-typed anodes for alkali metal-ion batteries, Small 17 (2021), 2005745.

[39] S.K. Park, Y.C. Kang, MOF-templated N-doped carbon-coated $CoSe_2$ nanorods supported on porous CNT microspheres with excellent sodium-ion storage and electrocatalytic properties, ACS Appl. Mater. Interfaces 10 (20) (2018) 17203–17213.

[40] C. Cui, Z. Wei, G. Zhou, W. Wei, J. Ma, L. Chen, C. Li, Quasi-reversible conversion reaction of $CoSe_2$/nitrogen-doped carbon nanofibers towards long-lifetime anode materials for sodium-ion batteries, J. Mater. Chem. A 6 (2018) 7088.

[41] H. He, D. Huang, Q. Gan, J. Hao, S. Liu, Z. Wu, W. Pang, H. He, D. Huang, Q. Gan, J. Hao, S. Liu, Z. Wu, W. Johannessen, Y. Tang, J. Luo, H. Wang, Z. Guo, Anion vacancies regulating endows MoSSe with fast and stable potassium ion storage, ACS Nano. 13 (2019) 11843–11852.

[42] J.M. Wang, B.B. Wang, H.M. Sun, G. Wang, J.T. Bai, H. Wang, Heterogeneous interface containing selenium vacancies space-confined in double carbon to induce superior electronic/ionic transport dynamics for sodium/potassium-ion half/full batteries, Energy Storage Mater. 46 (2022) 394–405.

[43] J. Sun, Y. Hou, Z. Yu, L. Tu, Y. Yan, S. Qin, S. Chen, D. Lan, H. Zhu, S. Wang, Visible-light-driven Z-scheme $Zn_3In_2S_6$/AgBr photocatalyst for boosting simultaneous Cr(VI) reduction and metronidazole oxidation: kinetics, degradation pathways and mechanism, J. Hazard. Mater. 419 (2021), 126543.

[44] G. Yang, Y. Liang, Z. Xiong, J. Yang, K. Wang, Z. Zeng, Molten salt-assisted synthesis of Ce_4O_7/Bi_4MoO_9 heterojunction photocatalysts for photo-fenton degradation of tetracycline: enhanced mechanism, degradation pathway and products toxicity assessment, Chem. Eng. J. 425 (2021), 130689.

[45] T. Li, Y. Liu, M. Li, J. Jiang, J. Gao, S. Dong, Fabrication of oxygen defect-rich pencil-like ZnO nanorods with C Dots and Ag co-enhanced photocatalytic activity for tetracycline hydrochloride degradation, Sep. Purif. Technol. 266 (2021), 118605.

[46] S. Balu, Y.L. Chen, S.W. Chen, T.C.K. Yang, Rational synthesis of $Bi_xFe_{1-x}VO_4$ heterostructures impregnated sulfur-doped g-C_3N_4: A visible-light-driven type-II heterojunction photo (electro)catalyst for efficient photodegradation of roxarsone and photoelectrochemical OER reactions, Appl. Catal. B Environ. 304 (2022), 120852.

[47] B. He, S. Jia, M. Zhao, Y. Wang, T. Chen, S. Zhao, Z. Li, Z. Lin, Y. Zhao, X. Liu, General and robust photothermal-heating-enabled high-efficiency photoelectrochemical water splitting, Adv. Mater. 33 (16) (2021) 2004406.

[48] S.H. Chen, S. Gu, H.B. Zhu, K.Y. Gao, C.M. Zhang, W.L. Xu, X.F. Wang, Carbon nanotube/$ZnIn_2S_4$ nanocomposites with efficient spatial charge separation and migration for solar H_2 generation, ACS Appl. Nano Mater. 5 (5) (2022) 6474–6484.

[49] S. Feng, M.G. Yu, T.P. Xie, T. Li, D.S. Kong, J.W. Yang, C.L. Cheng, H.Y. Chen, J. K. Wang, MoS_2/$CoFe_2O_4$ heterojunction for boosting photogenerated carrier separation and the dominant role in enhancing peroxymonosulfate activation, Chem. Eng. J. 433 (1) (2022), 134467.

[50] Y.Y. Yao, C.H. Wang, X. Yan, H. Zhang, C.M. Xiao, J.W. Qi, Z.G. Zhu, Y.J. Zhou, X. Y. Sun, X.G. Duan, J.S. Li, Rational regulation of Co−N−C coordination for high-efficiency generation of $^1O_2$ toward nearly 100% selective degradation of organic pollutants, Environ. Sci. Technol. 56 (12) (2022) 8833–8843.

[51] W. Chen, P. Westerhoff, J.A. Leenheer, K. Booksh, Fluorescence excitation-emission matrix regional integration to quantify spectra for dissolved organic matter, Environ. Sci. Technol. 37 (2003) 5701–5710.

[52] K. Qian, H. Chen, W.L. Li, Z.M. Ao, Y.N. Wu, X.H. Guan, Single-atom Fe catalyst outperforms its homogeneous counterpart for activating peroxymonosulfate to achieve effective degradation of organic contaminants, Environ. Sci. Technol. 55 (10) (2021) 7034–7043.

[53] J. Li, W.F. Huang, L.X. Yang, G. Gou, C.Y. Zhou, L.G. Li, N.W. Li, C. Liu, B. Lai, Novel Ag_3PO_4 modified tubular carbon nitride with visible-light-driven peroxymonosulfate activation: a wide pH tolerance and reaction mechanism, Chem. Eng. J. 432 (15) (2022), 133588.

[54] Y. Yang, G. Banerjee, G.W. Brudvig, J.H. Kim, J.J. Pignatello, Oxidation of organic compounds in water by unactivated peroxymonosulfate, Environ. Sci. Technol. 52 (10) (2018) 5911–5919.

[55] Q.L. Xu, L.Y. Zhang, B. Cheng, J.J. Fan, J.G. Yu, S-scheme heterojunction photocatalyst, Chem 6 (7) (2020) 1543–1559.

[56] P.F. Xia, S.W. Cao, B.C. Zhu, M.J. Liu, M.S. Shi, J.G. Yu, Y.F. Zhang, Designing a 0D/2D S-scheme heterojunction over polymeric carbon nitride for visible-light photocatalytic inactivation of bacteria, Angew. Chem. Int. Ed. 59 (13) (2020) 5218–5225.

[57] W.R. Liao, W. Qi, Y.L. Wang, J.Y. Qin, G.Y. Liu, S.J. Liang, H.Y. He, L.L. Jiang, Interfacial engineering promoting electrosynthesis of ammonia over Mo/ Phosphotungstic acid with high performance, Adv. Funct. Mater. 31 (22) (2021), 2009151.

[58] Y. Li, J. Qian, M. Zhang, S. Wang, Z. Wang, M. Li, Y. Bai, Q. An, H. Xu, F. Wu, L. Mai, C. Wu, Co-construction of sulfur vacancies and heterojunctions in tungsten disulfide to induce fast electronic/ionic diffusion kinetics for sodium-ion batteries, Adv. Mater. 32 (2020), 2005802.

[59] J. Lee, U. Von Gunten, J.H. Kim, Persulfate-based advanced oxidation: critical assessment of opportunities and roadblocks, Environ. Sci. Technol. 54 (2020) 3064–3081.

[60] V.L. Deringer, A.L. Tchougréeff, R. Dronskowski, Crystal orbital Hamilton population (COHP) analysis as projected from plane-wave basis sets, J. Phys. Chem. A 115 (2011) 5461–5466.

[61] X. Gao, J. Chen, H.N. Che, Y.H. Ao, P.F. Wang, Rationally constructing of a novel composite photocatalyst with multi charge transfer channels for highly efficient sulfamethoxazole elimination: Mechanism, degradation pathway and DFT calculation, Chem. Eng. J. 426 (2021) 131585.